Tire-derived Carbon Composite Anodes for Sodium-ion Batteries

Yunchao Li[a,b], M. Parans Paranthaman[a,b*], Kokouvi Akato[b,c], Amit K. Naskar[b,c], Alan M. Levine[e], Richard J. Lee[e], Sang-Ok Kim[d], Jinshui Zhang[a], Sheng Dai[a], and Arumugam Manthiram[d]

[a] Chemical Sciences Division, Oak Ridge National Laboratory, Oak Ridge, Tennessee 37831, United States

[b] The Bredesen Center for Interdisciplinary Research and Graduate Education, The University of Tennessee, Knoxville, Tennessee 37996, United States

[c] Materials Science and Technology Division, Oak Ridge National Laboratory, Oak Ridge, Tennessee 37831, United States

[d] Materials Science and Engineering Program & Texas Materials Institute, The University of Texas at Austin, Austin, Texas 78712, United States

[e]RJ Lee Group, Monroeville, PA 15146, USA

*Corresponding author:

M. P. Paranthaman (paranthamanm@ornl.gov) Tel.: (865) 574-5045 Fax: (865) 574-4961

Abstract

Hard-carbon materials are considered as one of the most promising anodes for the emerging sodium-ion batteries. Here, we report a low-cost, scalable waste tire-derived carbon as an anode for sodium-ion batteries (SIBs). The tire-derived carbons obtained by pyrolyzing the acid-treated tire at 1100 ℃, 1400 ℃ and 1600 ℃ show capacities of 179, 185 and 203 mAh g^{-1}, respectively, after 100 cycles at a current density of 20 mA g^{-1} in sodium-ion batteries with good electrochemical stability. The portion of the low-voltage plateau region in the charge-discharge curves increases as the heat-treatment temperature increases. The low-voltage plateau is beneficial to enhance the energy density of the full cell. This study provides a new pathway for inexpensive, environmentally benign and value-added waste tire-derived products towards large-scale energy storage applications.

Keywords

Sodium-ion batteries (SIBs); tire-derived carbon; tire recycling; low-cost anodes

Introduction

With the concerns of the limited global availability of lithium resources and high cost, sodium-ion batteries (SIBs) are considered to be an alternative to lithium-ion batteries (LIBs), especially for applications where energy density are of minor importance, such as stationary grid energy storage of electricity produced from renewable sources [1, 2]. Due to its high abundance, low cost, and suitable working chemical potential (-2.7 V vs. Standard Hydrogen Electrode), rechargeable sodium-ion batteries are gradually attracting a lot of attention [3]. Sodium shares many similar chemical properties with lithium because of its location in the periodic table and the similarities of fundamental principles of SIBs and LIBs. Thus far, several suitable cathode materials have been developed for SIBs [4-7]. However, the absence of good anode material hinders the application of SIBs. The search for suitable electrode materials for sodium-ion batteries, in particular robust anodes for Na^+ storage therefore is of great importance and becomes more urgent. Extensive research has been conducted to develop potential materials, such as alloy anodes [8], conversion anodes [9, 10], insertion anodes [11] and carbon anodes. But on the way to commercialize SIBs, carbon based materials have attracted the most attention, respecting to their unique electrochemistry functions and low cost for large-scale application [12]. Compared to carbon anodes, the disadvantages of alloy anodes and conversion anodes for SIBs should be attributed to the large volume changes during sodiation and desodiation, which causes fast capacity fade. In addition, conversion anodes also encounter relative high working potential and the large hysteresis between discharge and charge problems. For intercalation anodes, the low capacity limits their application.

Unlike the successful application of graphite as anodes in LIBs, the electrochemical sodium insertion into graphite to form binary intercalation compound is proven to be not favorable [13, 14]. Theoretical calculations suggest that the interlayer distance of graphite is too small to accommodate the large Na^+ ion, and a minimum interlayer distance of 0.37 nm is believed to be good for Na^+ insertion [15]. Very recently, progress has been made by Adelhelm et al. through the use of solvent co-intercalation to address the unfavorable graphene layer intercalation [16]. A variety of carbon materials have been investigated as anodes for SIBs, such as hard carbons [17], carbon nanotubes [15], reduced graphene oxides [18], and expanded graphite [19]. Hard carbon is likely to be the most promising anode for commercialization because of its stability, relatively high capacity and easy to scale-up. However, great amounts of the currently studied hard carbon are produced from sucrose [20], banana peels [21] and dopamine [22] *etc*. Most of the precursors are relatively high cost or require complex treatments, which prevent the application in many cost sensitive fields [23]. A low-cost hard carbon anode material is desired for promoting the development of SIBs for large-scale energy storage market.

The widespread use of motor vehicles unavoidably results in large quantities of used tires. Globally, it is estimated that about 1.5 billion waste tires are produced every year [24]. In the past, used tires are mostly disposed in landfills, which is not a sustainable solution. As more and more discoveries find that discarded tires pose serious environmental and health threats to our society, proper recycling of worn-out tires has become a critical issue. By now, the recycling of tires was mainly consumed as fuel, additives to plastics, rubbers, or civil engineering applications. Typically, a tire consists of natural rubber, synthetic polyisoprene, butadiene rubber, styrene-butadiene rubber,

carbon black and a fractional amount of additives [25]. The regular direct pyrolysis process results in the production of about 30-40% carbon black, depending on the pyrolysis conditions [24]. A high value-added product produced from used tires will lead more opportunities for the recycling industry and generate more environmental and economic benefits.

Tires are designed to be stable in physical and chemical harsh conditions owing to their cross-linked structure and various additives, which make them hard for recycling. However, such disadvantages are also the desired properties for electrochemical energy storage applications. A method for producing sulfonated and pyrolyzed carbon composite from recycled micronized tire rubber has been reported [26, 27]. The sulfonated tire-derived carbon has ~10% higher yield than the controlled carbon that was produced from the direct pyrolysis of powder rubber. Since the vulcanized tire formulation consists of a mixture of diene-rubbers such as polybutadiene, polyisoprene, or styrene-butadiene copolymer, desulfonation of rubbers or aliphatic hydrocarbon during the pyrolysis step will form unsaturated moieties that are relatively better char-forming materials [26]. This process also improves the carbon yields. Relatively low packing density and higher operating voltage are among the main obstacles for hard carbons to be used as an anode in LIBs. However, such problem will not be a big issue for SIB application since sodium-ion batteries are mostly targeted for stationary energy storage and also the Na/Na^+ couple operates 0.34 V higher than Li/Li^+ couple. To validate our hypothesis on potential use of tire-derived carbons in SIB anodes we present here the performance of these carbons, synthesized at different temperatures. Interestingly, a higher temperature of pyrolysis leads to a larger sodium storage capacity, which behaves opposite to that of some hard

carbons produced in the same temperature range and used against lithium. In the meanwhile, unlike most hard carbon voltage profile in LIBs, the plateau capacity at low-potential region increases significantly as the pyrolysis temperature increases, which is beneficial to increase the cell voltage and energy density.

Experimental Details

Tire-derived Carbon Synthesis

Pulverized tire rubber powder in the size range of 80–120 μm was obtained from Lehigh Technologies, Inc., Georgia. Typically, 50g of tire rubber powders were soaked in a 100 mL concentrated sulfuric acid bath (kept at 110 ºC for overnight) to yield the sulfonated tire rubber which was then washed and filtered off. The washed sulfonated tire rubber was then pyrolyzed from room temperature to 400 ºC at a ramp rate of 1 ºC /min and then the temperature was further increased to 1100 ºC, 1400 °C, and 1600 ºC, respectively at a ramp rate of 2 ºC /min, in a tube furnace under flowing nitrogen gas, and they are hereafter designated as TC1100, TC1400, and TC1600. Currently, the reported synthesis method can be scaled up to produce nearly 500g of materials in a batch and soon will be scale-up to few kg of materials.

Material Characterization

The X-ray diffraction (XRD) data were collected with a PANalytical Empyrean diffractometer equipped with Cu Kα radiation (λ=1.5406Å). Nitrogen adsorption desorption isotherms were obtained with a Quantachrome NovaWin1000 surface area & porosity analyzer at 77.4° K. The specific surface area was determined by the Brunauer-Emmett-Teller (BET) method. The pore size distribution was obtained by the Barret-

Joyner-Halenda (BJH) method. Raman spectra were collected with a Horiba LabRam HR using an excitation wavelength of 473nm, a 600 gr/mm grating and an 800 mm monochromator. A Zeiss Merlin VP scanning electron microscope (SEM) operated at 3kV was used to characterize the surface morphologies of the samples. Interlayer distances of the carbons were determined by a Hitachi HD-2300A scanning transmission electron microscope (STEM) with a field emission source operated at 200 kV in bright-field imaging mode at a 2.1Å resolution. XPS data were collected with a Thermo-Fisher K-alpha XPS with a monochromatic Al-K_{alpha}, a 1486.6 eV source, 400 µm spot, and an argon ion flood gun.

Electrochemical Measurements

Electrochemical properties were characterized with half cells against a sodium-metal electrode. The working electrode was prepared by spreading the mixed slurry consisting of the active material, conductive carbon C45 and PVDF binder in N-methyl-2-pyrrolidone (NMP) solvent at a weight ratio of 80:10:10. The resulting slurry was then casted onto a copper foil current collector and transferred to a vacuum oven for drying at 120 °C overnight. The typical loading amount of active material was 2 to 2.5 mg cm^{-2}. The electrolyte was a solution of 1 M $NaClO_4$ in ethylene carbonate (EC) and diethyl carbonate (DEC) (1:1 in vol). Coin cells (CR2032) consisting of the tire-derived carbon electrode, glass fiber, a sodium metal counter electrode and electrolyte were assembled in an Ar-filled glove box. Galvanostatic charge/discharge was carried out on a Land CT2001 battery test system (Wuhan, China) over a voltage range of 0 – 3 V at current density of 20 mA g^{-1} at room temperature. The sodiated electrodes were disassembled in an Ar-filled glovebox and placed in an air-sensitive sample holder for further

characterizations. The *ex situ* XRD analysis was performed on a Rigaku Miniflex600 diffractometer with Cu Kα radiation.

Results and Discussion

As shown in **Figure 1(a)**, XRD collected on bulk materials indicate that the tire-derived carbons pyrolyzed at different temperatures are mainly composed of poorly crystalline carbonaceous material. The broad peak near $2\theta \sim 26.6°$ suggests lack of significant order in the bulk of the carbon materials and this peak is related to the (002) plane. The R value for TC1100, TC1400, and TC1600 are 1.58, 2.27 and 2.67, respectively. Here, R is defined as the peak height divided by the background height at the position of the peak. The value of R can be used to estimate the fraction of graphene sheets, which increases as the proportion of the graphene layers with parallel neighbors increases [28]. TC1600 shows the largest graphene fraction by the comparing three R values. Raman spectra obtained on tailored carbons are shown in **Figure 1(b)**. The I_D/I_G ratio for TC1100, TC1400, and TC16000 increases from 0.85 to 0.96 to 0.99. Such a trend has also been reported for hard carbon material obtained from other precursors [29]. The I_D/I_G ratio changes differently in a three-stage model of increasing disorder as illustrated by Ferrari et al [30]. The G peak is due to the bond stretching of all pairs of sp^2 atoms in both rings and chains. The D peak is due to the breathing modes of sp^2 atoms in the rings. The ratio of I_D/I_G is proportional to the number of aromatic rings [31]. The increased relationship in the I_D/I_G ratio and G band position for the tire-derived carbons shows that more sp^2 amorphous carbon turns into nanocrystalline graphite at higher temperatures. This tendency can also be concluded and confirmed by the R values.

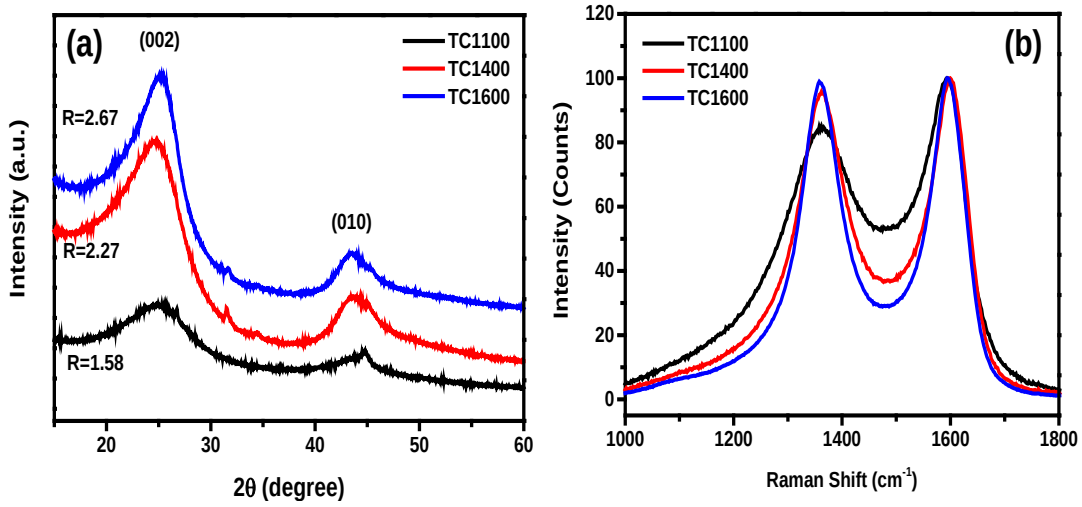

Figure 1. (a) X-ray diffraction patterns and (b) Raman spectra of tire-derived carbons obtained by pyrolyzing at different temperatures.

Nitrogen adsorption–desorption plots for the sulfonated tire rubber-derived carbons are plotted in **Figure S1 (a)** and the pore volume distribution is shown in **Figure S1 (b)**. The BET surface areas of TC1100, TC1400, and TC1600 are 189, 210 and 148 m^2 g^{-1}, respectively. The pore volume distribution shows a relatively wide pore size distribution with prominent microporosity with a pore width of less than 2 nm and a noticeable volume fraction of pore widths in the range of 6 - 8 nm. The dominant microporosity could be attributed to the fact that the sulfuric acid pretreated tire powder produces SO_2 and steam which yields activated tire-derived carbon [26]. The SEM images of different temperature treated tire-derived carbons exhibit similar surface porosity properties. Representative SEM images of TC1400 are shown in **Figure S2** as an example, where a large number of macro- and meso-pores are visible on the sample surface. High resolution scanning transmission electron microscopy (STEM) images of sulfonated tire-derived carbon treated at 1100°C, 1400 °C and 1600 °C are presented in **Figure S3**. The interlayer distances for crystalline areas were determined to be 4.7 Å, 4.5

Å, and 4.0 Å for TC1100, TC1400 and TC1600, respectively. These values are larger than the required distance (0.37 nm) [15] for sodium intercalation and follow the general trend that the carbon interlayer distance decreases with increasing pyrolysis temperatures. The selected area electron diffraction (SAED) patterns of the three temperature treated carbon indicate that the amorphous phase dominates. It is also clear that the TC1600 carbon has more crystalline phases compared to the lower temperature pyrolyzed carbon.

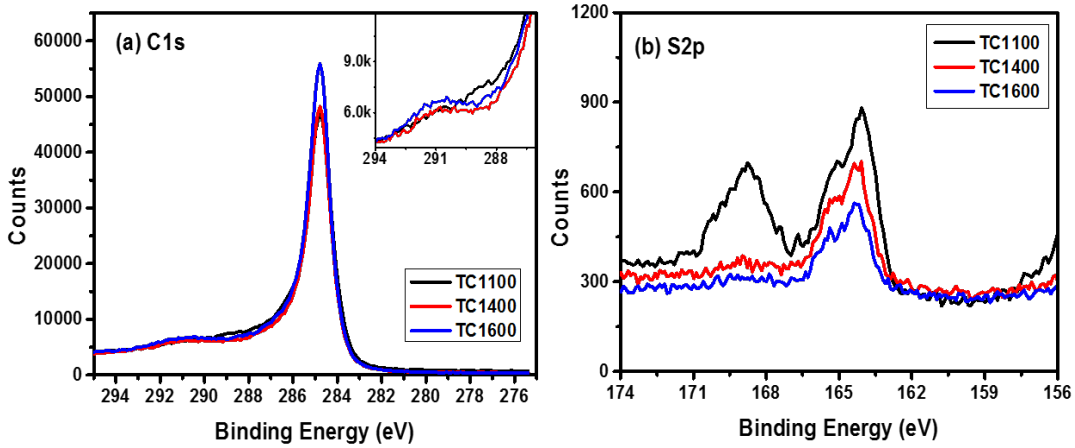

Figure 2. X-ray photoemission spectroscopy (XPS) of sulfonated tire rubber-derived carbons (a) C1s scans (b) S2p scans. The insert in (a) shows the expanded binding energy plots.

X-ray photoemission spectroscopy (XPS) of the tire-derived carbons are shown in **Figure 2**. The C1s spectrum in **Figure 2(a)** for the samples shows a sharp peck at 284.8 eV, which is due to the sp^2 configuration. The fitting results for C1s spectrum also show small amounts of C-O, C=O, and aromatic C functional groups on the surface. The small peak at around 291 eV could be related to the presence of aromatic rings in the materials and as shown in the inset that its relative intensity increases with the pyrolysis temperatures. This result also confirms the conclusion by Raman spectra that more

aromatic rings are present in the higher temperature samples. **Figure 2(b)** shows the S2p scans of the samples. The doublets at about 164 eV are related to the thiol group and the peak at 169 eV is due to the sulfate group. It is shown that as the temperature increases, sulfate groups are removed from the samples. The XPS elemental analysis for the samples is shown in **Table 1**. The impurities of Si and Fe could be due to the additives or impurities present in the tire powders. It is clear that the purity improves as the pyrolysis temperature increases since more functional groups are eliminated at higher temperatures.

Table 1. XPS surface concentration (in atomic percentages) of TC1100, TC1400 and TC1600.

Sample	Si	S	C	O	Fe
TC1100	1.5	1.1	82.1	14.8	1.52
TC1400	0.9	0.6	92.6	4.4	-
TC1600	0.5	0.5	95.5	3.6	-

The electrochemical performances of tire-derived carbons were evaluated in sodium half cells. **Figure 3** (a)-(c) show the cycling stability of the three samples tested under a current density of 20 mA g^{-1}. TC1100 provides an initial capacity of 520 mAh g^{-1} for discharge and 250 mAh g^{-1} during charge, which corresponds to only 48% coulombic efficiency for the first cycle in **Figure 3 (a)**. The large irreversible capacity loss could be associated with the high surface area of the carbon material and the reduction of carbon surface functional groups followed by electrolyte decomposition and formation of solid electrolyte interphase (SEI) [32, 33]. Surface coating techniques could be used in the future to reduce the surface area and to improve the efficiency. After the 10^{th} cycle, the

coulombic efficiency increases to above 99% and the capacity becomes stabilized. The capacity at the 100th cycle was 179.4. Compared to TC1100, the cycling results for TC1400 and TC1600 in **Figure (b) and (c)** show improvements in first cycle efficiency and capacity. TC1400 exhibits 57% first cycle efficiency and a capacity of 185 mAh g^{-1} after 100 cycles whereas TC1600 shows further enhancement of the first cycle efficiency to 66% and a capacity of 203 mAh g^{-1} at 100th cycle. The improved cycling performance may be related to the reduced number of surface functional groups and also reduced amount of defects in the carbon after the higher temperature treatment.

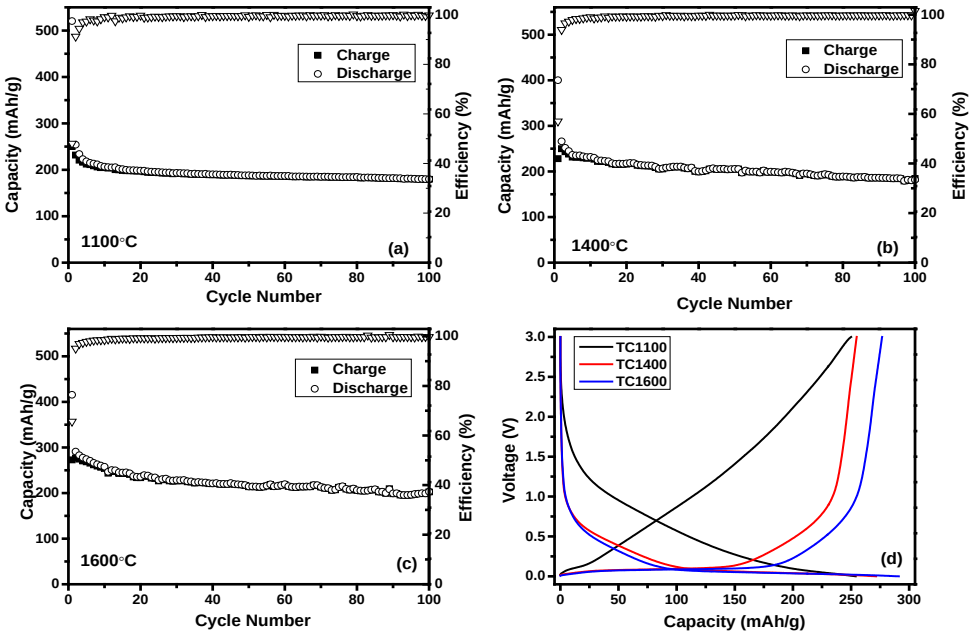

Figure 3. Cycling performances of (a) TC1100, (b) TC1400, and (c) TC1600, and (d) a comparison of discharge and charge curves of all the carbons.

Figure 3 (d) presents the electrochemical voltage profiles when sodium is intercalated and deintercalated from the various tire-derived carbons. It can be seen that the TC1100 voltage profile mostly consists of the sloping region during cycling.

However, both the TC1400 and TC1600 charge and discharge curves can be divided into two regions, a sloping voltage region extending down to 0.2 V and a large portion of the plateau region. Similar voltage profiles of other high temperature treated carbon materials for sodium-ion batteries have also been reported previously [29, 34, 35]. The observed charge capacity of the plateau region for TC1400 is 165 mAh g^{-1}, which is approximately 65% of the whole capacity. For TC1600, the plateau capacity increases to 197 mAh g^{-1}, accounting for 71% of the total capacity. In carbon materials, the disordered graphene layers are randomly distributed and can be modeled like a “house of cards” [28]. Steve et al. revealed that the sloping region of the potential profile corresponds to the insertion of sodium between the turbostratically disordered graphene layers and the low-potential plateau region can be attributed to the insertion of the metal into the nanopores between randomly stacked layers through a process analogous to adsorption [14]. When sodium is intercalating into graphene inter-layers continuously, the overall potential decreases as the insertion of metal ions between layers changes the potential for further insertion and turbostratic stacking between the parallel sheets gives rise to a distribution of insertion-site potentials [17]. The Na chemical potential of the following step in the pore filling is close to that of the elemental sodium metal, which shows a voltage plateau close to 0 V. The improved performance of tire-derived carbon at higher firing temperature suggests that more nano-crystalline graphene layers are created and these randomly stacked layers generate more voids for sodium storage at an elevated temperature. The increased capacities below 0.2 V for the tire-derived carbon could be attributed to the increase of nanopores (as shown in Figure S2) to provide more sites for sodium plating in the low potential region. Predominant amount of micropores below 2 nm increase as the

pyrolyzing temperature increases which suggests more SO_2 related activation occurred at higher temperatures.

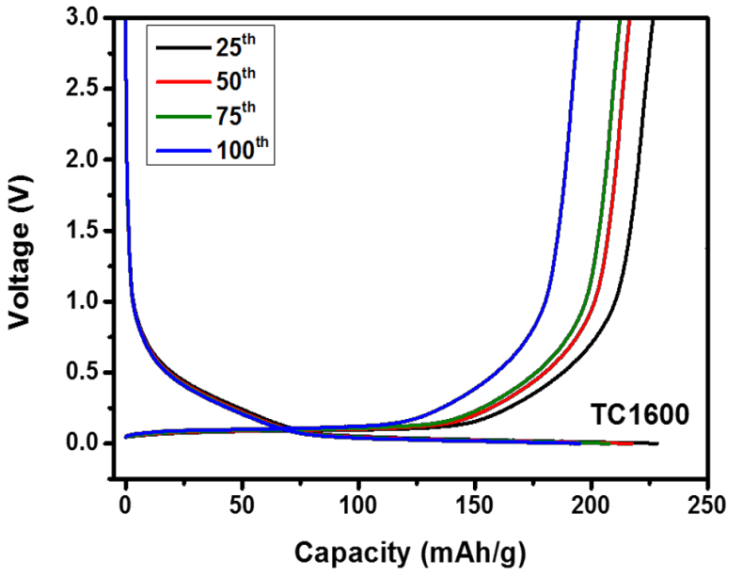

Figure 4. Comparison of the discharge and charge curves of TC1600 at 25th, 50th, 75th, and 100th cycles.

A comparison of the discharge and charge curves of TC1600 at different cycles is shown in **Figure 4**. The plot shows that the capacity decreases with cycling. However, by comparing the discharge capacity profile, it is interesting to reveal that the sloping region is almost constant while the plateau region is reduced dramatically. This rapid plateau region decay indicates the sodium adsorption-desorption in the nanopores at the low-potential region and hence capacity fades and the Na plating into nanopores is not fully reversible or has poor kinetic properties.

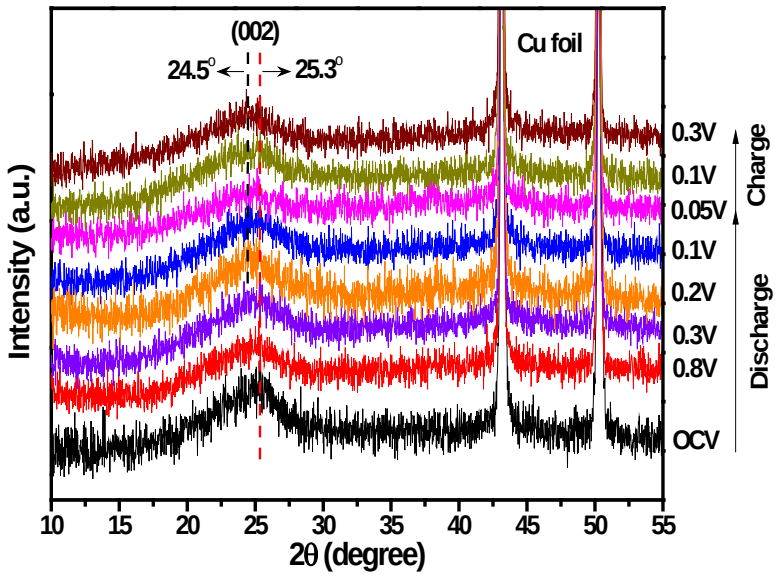

Figure 5. *Ex-situ* XRD patterns of the TC1600 electrodes at different voltages. Red dash line marker indicates the pristine material and black dash line marker indicates charged materials with a peak shift at low voltage.

Ex-situ XRD measurements (in **Figure 5**) were carried out to analyze the structural changes during sodium insertion into TC1600 carbon. For the pristine electrode, the (002) peak centered at 25.3º and the two strong peaks located between 40º and 55º are due to the copper foil substrate. All the patterns were adjusted based on the standard 2θ position of Cu as the internal standard. The coin cells were discharged from OCV to 0.8V, 0.3V, 0.2V, 0.1V, 0.05V and charged back to 0.1V and 0.3V, respectively. As sodium intercalates into the carbon electrode, the (002) peak shifts slightly to lower angle for electrodes discharged to lower voltage. Such peak shifts to lower angle indicates an increase in d-values due to sodium insertion between the parallel graphene-like layers and an expansion of the interlayer spacing. It is noticeable that the peak positions didn't change once discharged below 0.3V and stay unchanged even when it is charged back to 0.3V. This confirms the sodiation mechanism at low voltage changes from insertion between the parallel graphene-like layers to the filling of sodium into nanopores in the

materials. It is also interesting to mention that Tarascon *et al.* recently reported in-situ XRD results for sodiation process for carbon nanofibers heat treated at 2200 ºC [36]. No (002) peak shift was observed during the sodiation and desodiation process and this observation is different from our results and also some previously reported results[14, 34]. Such a difference could be possibly attributed by much higher treatment temperature for their samples, which would greatly reduce the interlayer distance between parallel graphene layers and makes it impossible for Na^+ to intercalate between the layers.

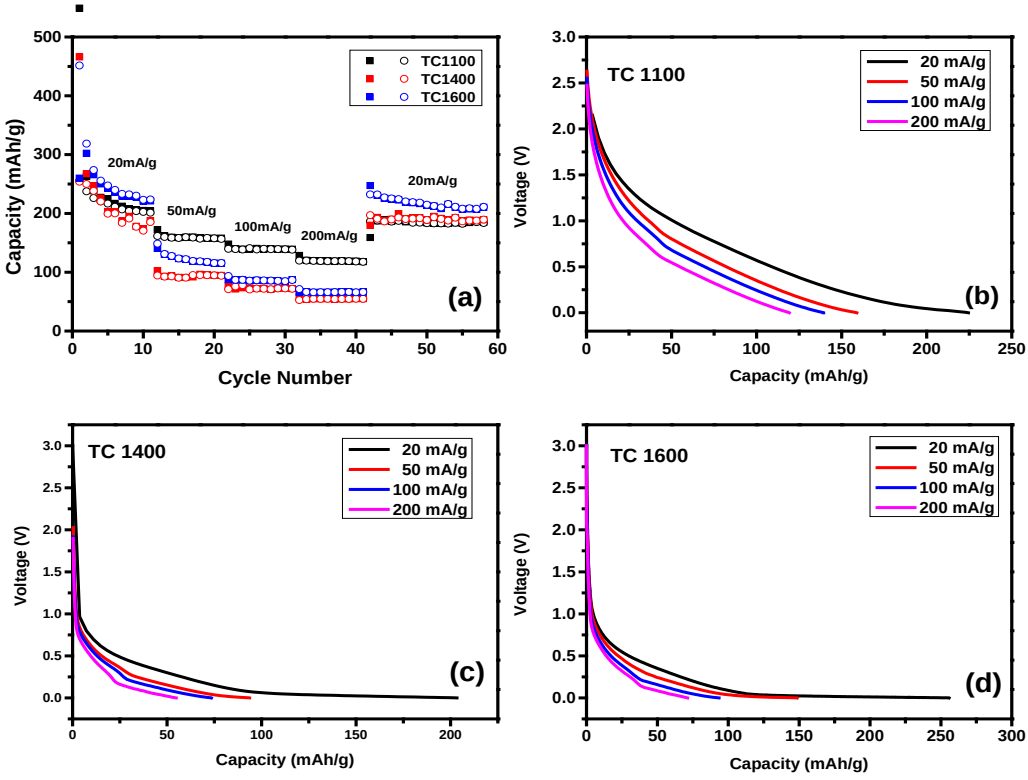

Figure 6. (a) Cycling capacities of TC1100, TC1400, and TC1600 at different current densities, and discharge profiles of (b) TC1100, (c) TC1400, and (d) TC1600 at different current densities.

Figure 6 shows the charge and discharge capacities of TC1100, TC1400 and TC1600 at different current densities. As shown in **Figure 6 (a)**, TC1600 has the highest capacity at a small current density (20 mA/g). However, as the current density increases,

both TC1600 and TC1400 suffer from dramatic capacity fade, dropping from 256 mAh/g at 20 mA/g to 72 mAh/g at 200 mA/g for TC1600 and from 204 mAh/g at 20 mA/g to 55 mAh/g at 200 mAh/g for TC1400. Meanwhile, TC1100 exhibits much better large-current-density tolerance which has a capacity of 225 mAh/g at 20 mA/g and maintains 120 mAh/g at 200 mAh/g. **Figure 6 (b), (c)** and **(d)** are plotted for comparing the discharge voltage profiles for all carbon samples at different current densities and they reveal the possible reasons. As discussed before, both TC1400 and TC1600 have a larger portion of the low-voltage plateau, which is caused by pore plating of sodium metal. This plateau rapidly disappears as the current density increases. TC1100 does not have a plateau and delivers a larger capacity at higher current density. These results indicate that the pore plating process will be slower and needs more time to reach equilibrium than the sodium insertion into disordered graphene layers. To further improve the high rate capability, electrode materials conductivity could be improved with a surface coating process [29].

The long-term stability test was conducted for TC1100 in 1M $NaClO_4$ in propylene carbonate (PC) as the electrolyte, as shown in **Figure 7**. Good cyclability performance proves that the materials could also work in other electrolytes, such as PC based systems, which can be operated at lower temperature than ethylene carbonate (EC) based electrolytes. TC1100 shows a capacity of 154 mAh g^{-1} after 600 cycles at a current density of 20 mA g^{-1}.

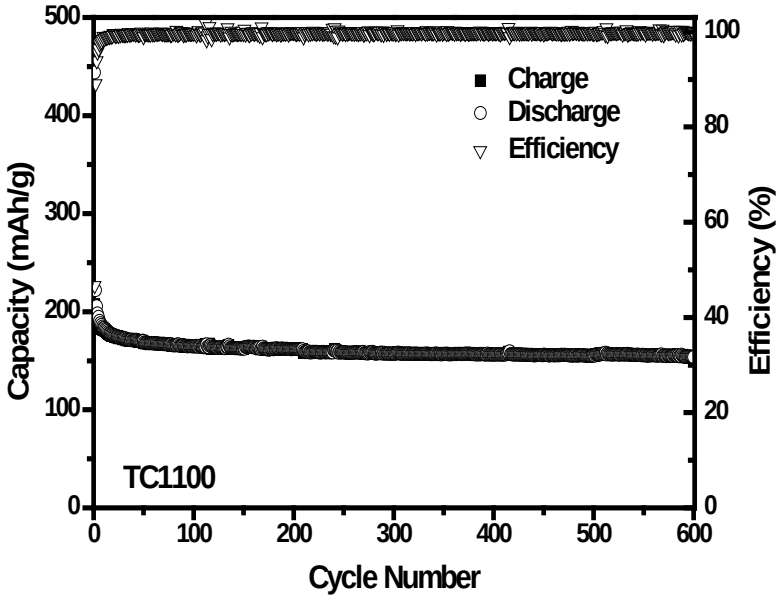

Figure 7. Long-cycle stability test of TC1100 at a current density of 20 mA g^{-1}.

A comparison table of the recently reported carbon materials for sodium ion batteries along with our results is shown in **Table 2**. As it can be seen, tire-derived carbons have comparable performances with most of the state-of-art sodium ion battery carbon electrodes. Considering the main advantage for SIBs is their low cost, especially for large-scale energy storage, cost is always the most important aspect. Many of the current well-performing materials use high value precursors such as dopamine, polyaniline nanowires and graphene oxides, which could hinder their potential for large scale applications. However, the cost for waste/recycled tires is even much lower than the most common used sucrose, which costs ~ $0.06 per kilogram with more than 70% yields for waste tire and $0.25 per kg with about 45% yields for sucrose [23]. Also, the waste tire recycling process is well-developed and the sources are readily available in large amounts compared to materials made with banana peels and peanut skin.

Table 2. Comparison of the sodium storage performance for state-of-the-art SIB carbons.

	Performance	1st cycle efficiency	Capacity below 0.2V vs Na/Na^+	Source
N-doped carbon sheets[22]	165 $mAhg^{-1}$ after 600 cycles (200 mAg^{-1})	26.4%	not reported	dopamine
Porous N-doped carbon sphere[37]	206 $mAhg^{-1}$ after 600 cycles (200 mAg^{-1})	39.9%	ca. 70 $mAhg^{-1}$ at 200 mAg^{-1} (3rd cycle)	polypyrrole
Banana peel pseudographite[21]	210 $mAhg^{-1}$ after 600 cycles (500 mAg^{-1})	67.8%	200 $mAhg^{-1}$ at 50 mAg^{-1} (10th cycle)	banana peel
Hollow carbon spheres[38]	160 $mAhg^{-1}$ after 100 cycles (100 mAg^{-1})	41.5%	ca. 100 $mAhg^{-1}$ at 50 mAg^{-1} (10th cycle)	D-glucose
Hard carbon spherules[20]	290 $mAhg^{-1}$ after 100 cycles (30 mAg^{-1})	83.0%	220 $mAhg^{-1}$ at 30 mAg^{-1} (2nd cycle)	sucrose
Carbon microspheres[39]	183 $mAhg^{-1}$ after 50 cycles (30 mAg^{-1})	ca. 40%	ca. 120 $mAhg^{-1}$ at 30 mAg^{-1} (2nd cycle)	sucrose
N-doped porous carbon sheets[40]	155.2 $mAhg^{-1}$ after 260 cycles (50 mAg^{-1})	34.9%	ca. 150 $mAhg^{-1}$ at 50 mAg^{-1} (5th cycle)	graphene oxides
Hollow carbon nanowires[41]	206.3 $mAhg^{-1}$ after 400 cycles (50 mAg^{-1})	50.5%	ca. 150 $mAhg^{-1}$ at 50 mAg^{-1} (2nd cycle)	polyaniline nanowires
Hierarchical porous carbons[42]	160 $mAhg^{-1}$ after 200 cycles (500 mAg^{-1})	34.0%	ca. 100 $mAhg^{-1}$ at 100 mAg^{-1} (10th cycle)	peanut skin
Present work	203 $mAhg^{-1}$ after 100 cycles (20 mAg^{-1})	66.0%	197 $mAhg^{-1}$ at 20 mAg^{-1} (3rd cycle)	waste tire

Conclusions

In summary, we have demonstrated the use of solid-waste-tire-derived carbons as anodes for sodium-ion batteries. When the pyrolysis temperature is increased from 1100 to 1600°C, the capacity of the plateau below 0.2 V increases dramatically and this could help increase the full cell energy density. The 1600°C treated carbon shows a capacity of 203 mAh g^{-1} after 100 cycles. These tire-derived carbons demonstrate a low-cost, easily scalable option with good electrochemical capacity and stability for sodium-ion battery anodes.

Acknowledgements

The evaluation of the new materials as novel battery electrodes was sponsored by the U.S. Department of Energy, Office of Science, Office of Basic Energy Sciences, Materials Sciences and Engineering Division. The research on the conversion of recycled tires to carbon powders was funded by Oak Ridge National Laboratory's Technology Innovation Program.

References

[1] D. Kundu, E. Talaie, V. Duffort, L.F. Nazar, Angew Chem Int Edit, 54 (2015) 3431-3448.
[2] S.-W. Kim, D.-H. Seo, X. Ma, G. Ceder, K. Kang, Advanced Energy Materials, 2 (2012) 710-721.
[3] H. Pan, Y.-S. Hu, L. Chen, Energy & Environmental Science, 6 (2013) 2338.
[4] B.L. Ellis, W.R.M. Makahnouk, Y. Makimura, K. Toghill, L.F. Nazar, Nature materials, 6 (2007) 749-753.
[5] M. Sathiya, K. Hemalatha, K. Ramesha, J.M. Tarascon, A.S. Prakash, Chemistry of Materials, 24 (2012) 1846-1853.
[6] H. Yoshida, N. Yabuuchi, K. Kubota, I. Ikeuchi, A. Garsuch, M. Schulz-Dobrick, S. Komaba, Chemical Communications, 50 (2014) 3677-3680.
[7] N. Yabuuchi, M. Kajiyama, J. Iwatate, H. Nishikawa, S. Hitomi, R. Okuyama, R. Usui, Y. Yamada, S. Komaba, Nature materials, 11 (2012) 512-517.
[8] Y.N. Ko, Y.C. Kang, Chem Commun, 50 (2014) 12322-12324.
[9] I. Hasa, R. Verrelli, J. Hassoun, Electrochimica Acta, 173 (2015) 613-618.
[10] F. Klein, B. Jache, A. Bhide, P. Adelhelm, Physical chemistry chemical physics : PCCP, 15 (2013) 15876-15887.
[11] M. Shirpour, J. Cabana, M. Doeff, Energ Environ Sci, 6 (2013) 2538-2547.
[12] C. Bommier, X. Ji, Israel Journal of Chemistry, 55 (2015) 486-507.
[13] P. Ge, M. Fouletier, Solid State Ionics, 28 (1988) 1172-1175.
[14] D.A. Stevens, J.R. Dahn, Journal of The Electrochemical Society, 148 (2001) A803.
[15] Y.L. Cao, L.F. Xiao, M.L. Sushko, W. Wang, B. Schwenzer, J. Xiao, Z.M. Nie, L.V. Saraf, Z.G. Yang, J. Liu, Nano Letters, 12 (2012) 3783-3787.
[16] B. Jache, P. Adelhelm, Angewandte Chemie, 53 (2014) 10169-10173.
[17] D.A. Stevens, J.R. Dahn, Journal of the Electrochemical Society, 147 (2000) 1271-1273.
[18] Y.X. Wang, S.L. Chou, H.K. Liu, S.X. Dou, Carbon, 57 (2013) 202-208.
[19] Y. Wen, K. He, Y. Zhu, F. Han, Y. Xu, I. Matsuda, Y. Ishii, J. Cumings, C. Wang, Nat Commun, 5 (2014) 4033.
[20] Y.M. Li, S.Y. Xu, X.Y. Wu, J.Z. Yu, Y.S. Wang, Y.S. Hu, H. Li, L.Q. Chen, X.J. Huang, J Mater Chem A, 3 (2015) 71-77.
[21] E.M. Lotfabad, J. Ding, K. Cui, A. Kohandehghan, W.P. Kalisvaart, M. Hazelton, D. Mitlin, ACS nano, 8 (2014) 7115-7129.
[22] F. Yang, Z. Zhang, K. Du, X. Zhao, W. Chen, Y. Lai, J. Li, Carbon, 91 (2015) 88-95.
[23] M. Zhi, F. Yang, F. Meng, M. Li, A. Manivannan, N. Wu, ACS Sustainable Chemistry & Engineering, 2 (2014) 1592-1598.
[24] B. Danon, P. van der Gryp, C.E. Schwarz, J.F. Görgens, Journal of Analytical and Applied Pyrolysis, 112 (2015) 1-13.
[25] A. Quek, R. Balasubramanian, Journal of Analytical and Applied Pyrolysis, 101 (2013) 1-16.
[26] A.K. Naskar, Z. Bi, Y. Li, S.K. Akato, D. Saha, M. Chi, C.A. Bridges, M.P. Paranthaman, RSC Advances, 4 (2014) 38213.
[27] M. Boota, M.P. Paranthaman, A.K. Naskar, Y. Li, K. Akato, Y. Gogotsi, ChemSusChem, (2015).
[28] J.R. Dahn, W. Xing, Y. Gao, Carbon, 35 (1997) 825-830.
[29] Y. Li, S. Xu, X. Wu, J. Yu, Y. Wang, Y.-S. Hu, H. Li, L. Chen, X. Huang, J. Mater. Chem. A, 3 (2015) 71-77.
[30] A.C. Ferrari, J. Robertson, Phys Rev B, 61 (2000) 14095-14107.

[31] A.C. Ferrari, J. Robertson, Philosophical Transactions of the Royal Society of London A: Mathematical, Physical and Engineering Sciences, 362 (2004) 2477-2512.
[32] J.R. Dahn, T. Zheng, Y.H. Liu, J.S. Xue, Science, 270 (1995) 590-593.
[33] E. Buiel, J.R. Dahn, Journal of The Electrochemical Society, 145 (1998) 1977-1981.
[34] S. Komaba, W. Murata, T. Ishikawa, N. Yabuuchi, T. Ozeki, T. Nakayama, A. Ogata, K. Gotoh, K. Fujiwara, Advanced Functional Materials, 21 (2011) 3859-3867.
[35] C. Bommier, T.W. Surta, M. Dolgos, X. Ji, Nano Lett, 15 (2015) 5888-5892.
[36] B. Zhang, C.M. Ghimbeu, C. Laberty, C. Vix-Guterl, J.-M. Tarascon, Advanced Energy Materials, 6 (2016) n/a-n/a.
[37] D. Li, H. Chen, G. Liu, M. Wei, L.-x. Ding, S. Wang, H. Wang, Carbon, 94 (2015) 888-894.
[38] K. Tang, L. Fu, R.J. White, L. Yu, M.-M. Titirici, M. Antonietti, J. Maier, Advanced Energy Materials, 2 (2012) 873-877.
[39] T. Chen, L. Pan, T. Lu, C. Fu, D.H.C. Chua, Z. Sun, J. Mater. Chem. A, 2 (2014) 1263-1267.
[40] H.G. Wang, Z. Wu, F.L. Meng, D.L. Ma, X.L. Huang, L.M. Wang, X.B. Zhang, ChemSusChem, 6 (2013) 56-60.
[41] Y. Cao, L. Xiao, M.L. Sushko, W. Wang, B. Schwenzer, J. Xiao, Z. Nie, L.V. Saraf, Z. Yang, J. Liu, Nano letters, 12 (2012) 3783-3787.
[42] H. Wang, W. Yu, J. Shi, N. Mao, S. Chen, W. Liu, Electrochimica Acta, 188 (2016) 103-110.

Supporting Information:

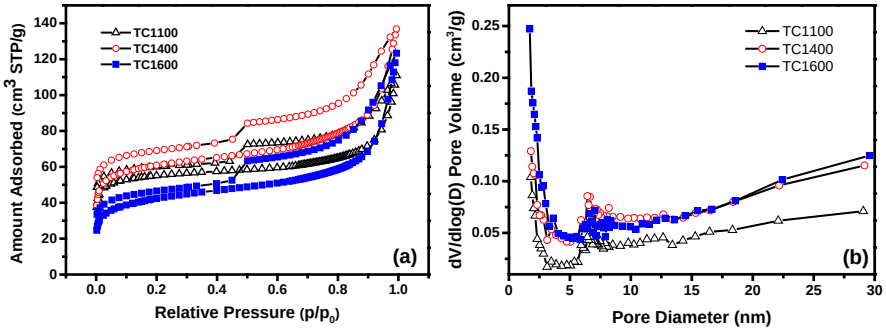

Figure S1. (a) BET and (b) pore volume distribution of TC1100, TC1400 and TC1600.

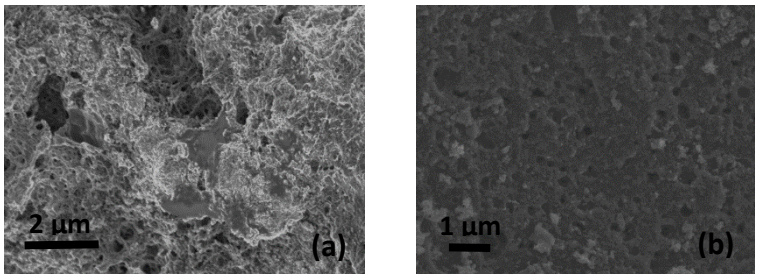

Figure S2. SEM images of TC1400 surface.

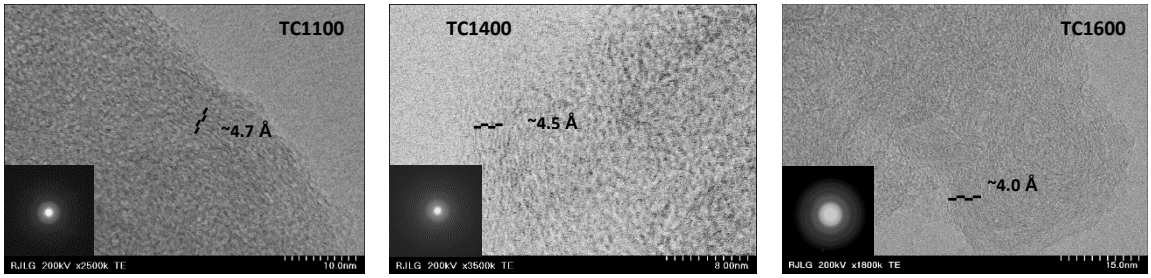

Figure S3. TEM images of TC1100, TC1400, and TC1600. The inset shows a selected area diffraction pattern of each carbon.